Chapter 1

Introduction

Transition metal dichalcogenides (TMds) are layered materials which are composed of transition metals (**Transition metal**, any of various chemical elements that have valence electrons—i.e., electrons that can participate in the formation of chemical bonds—in two shells instead of only one) and chalcogens (The chalcogens are the chemical elements in group 16 of the periodic table. This group is also known as the **oxygen** family. It consists of the elements oxygen, sulfur, selenium, tellurium, and the radioactive element polonium) of the group VIA in a 1:2 ratios [1]. TMds are among the most studied layered compounds that have been isolated in monolayer form. Compounds in the TMD family exhibit a wide range of electrical properties, depending on polytype and the number of transition metal d-electrons, and include metallic[2], half-metallic[3], semiconducting[4-5], superconducting[6], and charge density wave[7] behavior. Molybdenum and tungsten based TMDCs are semiconductors with band gaps ranging from the visible to the near infrared. Besides Mo and W, chalcogenides of Ti, Sn, and Zr are also predicted to be semiconducting but little to no experimental evidence exists on their isolation in monolayer form, stability, or performance in devices. Thus, Mo and W chalcogenides have been the most heavily investigated among the post-graphene two-dimensional materials [8].

1- Chemistry of TMDs

Chalcogenides are materials that contain chalcogen species. The term ‘chalcogen’ refers to group VI elements such as sulphur, selenium, and tellurium. around 1930, Wilhelm Blitz of the Institute of Inorganic Chemistry at the University of Hannover, Germany, and his colleagues were investigating the relationship between the physical properties of chemical elements and their position in the Periodic Table. It became useful to refer to certain groups of elements by characteristic names. However, the group of the elements O, S, Se, and Te lacked such a name. In about 1932, one of W. Blitz’s co-workers proposed the term ‘chalcogens’ for these elements and ‘chalcogenides’ for their compounds using the analogy with the well-known terms ‘halogens’ (‘salt formers’) and ‘halogenides’ for the neighboring elements in the Periodic Table [9];
According to the IUPAC definition [10], a transition metal is ‘an element whose atom has a partially filled d sub-shell, or which can give rise to cations with an incomplete d sub-shell’. Transition metals have the following general electronic configuration:

$$(n-1)d^{1-10}ns^{2}$$

In a transition metal, a set of six *s*, *p* and *d*-orbitals can be hybridized like the sp^3 hybridization to generate six equivalent orbitals directed to the vertices of an octahedron. In order to form six-fold coordinated geometry, either d^2sp^3 or sp^3d^2 hybridization is required.

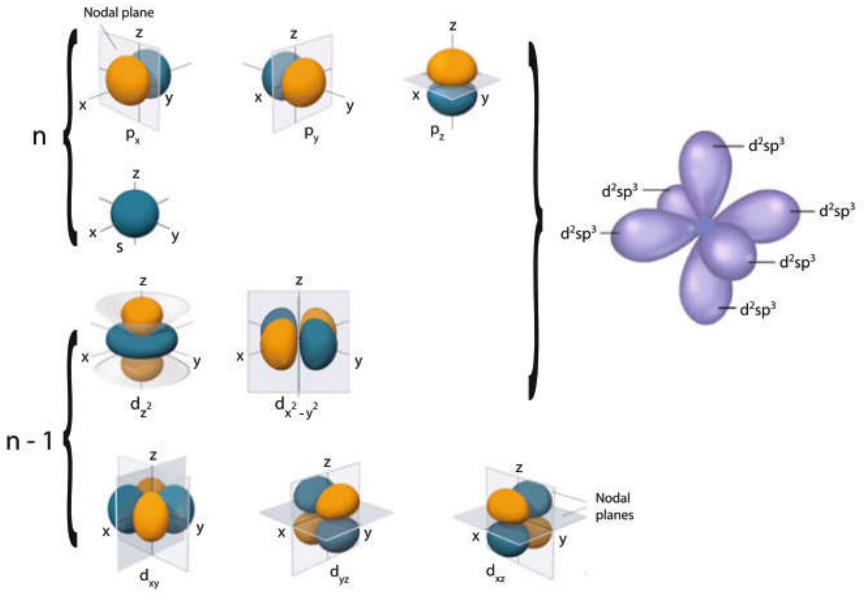

Fig. 1.1 Atomic *s*, *p*, and *d*-orbitals of a transition metal (*left*) (reproduced from [1]) and the corresponding set of d^2sp^3-hybridized orbitals (*right*) that allow for an octahedral bonding geometry of the metal.

While covalent bonds are typically formed between pairs of atoms each of which contributes one electron per bond, bonding in transition metal complexes is usually between vacant *d-s-p*-mixed (or hybridised) orbitals of the metal and LP electrons of ligands (Fig. 1.2, upper panel) giving rise to bonding and antibonding orbitals with σ symmetry around the metal-ligand bond axis. The resulting covalent bond is a dative bond, also called a coordinate covalent bond.

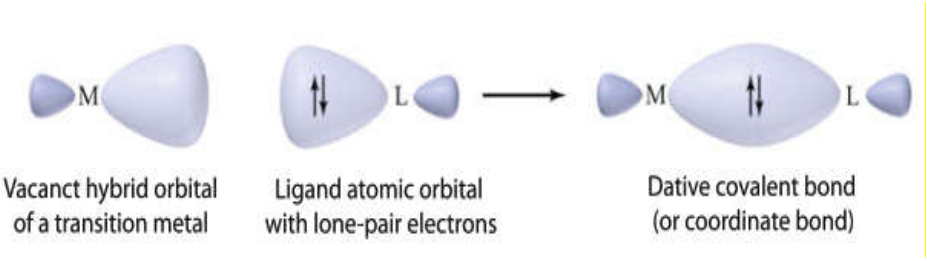

Fig. 1.2 *schematic* of the formation of a dative (coordination) bond between a vacant hybridised orbital of a transition metal and LP electrons of ligands.

2- TMDs Structures

Bulk (or 3D) TMDCs have been known and used for a very long time, but most of the older applications (i.e. as solid lubricants) were related to their unique mechanical properties determined by the presence of van der Waals bonding between the layers. It is only recently, following the success of graphene, that TMDCs moved to the forefront of solid-state research, with main interest being concentrated on mono and few-layer structures. Layered TMDCs have the generic formula MX_2, where M stands for a metal and X represents a chalcogen. In layered hexagonal structures six chalcogen atoms surround every metal atom. This arrangement yields

two possible structures: *trigonal* prismatic and *octahedral*. The interatomic interaction within layers is covalent in nature, while the layers are held together by weak van der Waals (vdW) forces.

The structure of a typical layered TMDC is shown in Fig. 1.3. In this structure, each layer consists of three atomic planes with a typical thickness of 6–7 Å with a hexagonally packed plane of metal atoms sandwiched between two planes of chalcogen atoms [9].

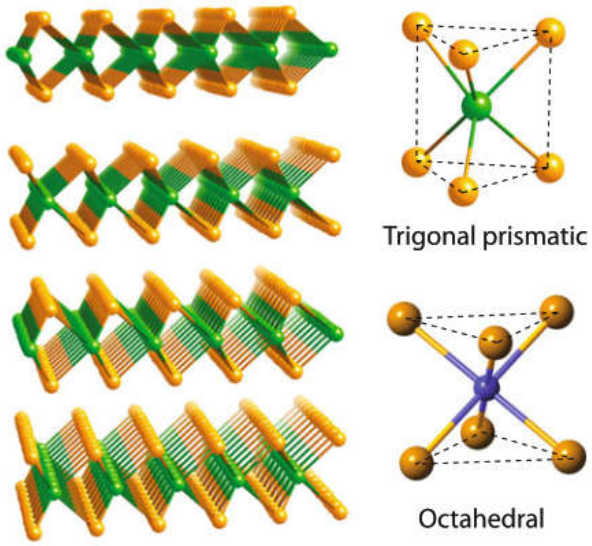

Fig. 1.3 Left a three-dimensional representation of a typical layered MX2 structure, with the metal atoms shown in green and the chalcogen atoms shown in orange. The local coordination of the metal species can be of the two types shown in the right panel, viz., trigonal prismatic (top) and octahedral (bottom).

Typically, ionic compounds prefer the octahedral coordination, while trigonal prismatic coordination is preferred for covalently bonded compounds. In trigonal prismatic structure, the two chalcogenide planes in a slab are stacked directly above each other forming trigonal interstices for metal atoms (D3h symmetry point group). Octahedral interstices (D3d symmetry point group) are formed for metal atoms, when the chalcogen planes are slightly tilted. These two types of atomic arrangements depend upon the nature of the bond formed between the metal and chalcogen atoms and could either exhibit semiconducting (e.g. MoS2, WS2, WSe2 and MoSe2, trigonal) or metallic-superconducting behavior (e.g. NbS2 and NbSe2, octahedral) [12].

3- Photoluminescence (PL) and Raman Spectroscopy

Photoluminescence spectroscopy is a contactless, nondestructive method of probing the electronic structure of materials. Light is directed onto a sample, where it is absorbed and imparts excess energy into the material in a process called photoexcitation. One way this excess energy can be dissipated by the sample is through the emission of light, or luminescence. In the case of photoexcitation, this luminescence is called photoluminescence [13].

Raman spectroscopy is a spectroscopic technique based on inelastic scattering of monochromatic light, usually from a laser source. Inelastic scattering means that the frequency

of photons in monochromatic light changes upon interaction with a sample. Photons of the laser light are absorbed by the sample and then reemitted. Frequency of the reemitted photons is shifted up or down in comparison with original monochromatic frequency, which is called the Raman effect. This shift provides information about vibrational, rotational and other low frequency transitions in molecules. Raman spectroscopy can be used to study solid, liquid and gaseous samples [14].

Bulk MoS2, a prototypical metal dichalcogenide, is an indirect bandgap semiconductor with negligible photoluminescence. When the MoS2 crystal is thinned to monolayer, however, a strong photoluminescence emerges, indicating an indirect to direct bandgap transition in this d-electron system. This observation shows that quantum confinement in layered d-electron materials like MoS2 provides new opportunities for engineering the electronic structure of matter at the nanoscale.

Layered transition metal dichalcogenides represent another class of materials, in which d-electrons' interactions can give rise to new physical phenomena. New researches show that MoS2 photoluminescence, surprisingly, increases with decreasing layer thickness, and that luminescence from a monolayer is the strongest while it is absent in bulk material [15].

For Raman scattering and photoluminescence measurements, we can use a 532 nm solid state laser to excite few-layers MoS2 on a Si/SiO2 wafer.

Figure 1.4 displays a photoluminescence spectrum of a monolayer MoS2. Pronounced luminescence emissions are observed at the A1 and B1 direct excitonic transitions. This photoluminescence emission in monolayer is in striking contrast to its absence in bulk MoS2, a consequence of bulk MoS2 being an indirect bandgap semiconductor like silicon.

In Figure 1.5, The photoluminescence spectra from monolayer, bilayer, hexalayer, and bulk MoS2 is shown. three prominent Raman modes can be identified in the spectra: the first peak corresponds to a MoS2 Raman excitation with a 408cm-1 Raman shift and the next two at 520 and 1030 cm-1 are the first and second order Raman peaks from the silicon substrate.

In bulk MoS2, no photoluminescence is observable, and the MoS2 Raman signal is weak because of the local field effect, that is, the local electric field at a high refractive index material like MoS2 is much weaker than the incident electrical field. For ultrathin MoS2 layers where local field effects are relatively small, the Raman and photoluminescence intensities show opposite layer dependence: MoS2 Raman signal is the weakest in the monolayer MoS2 (due to reduced amount of material), while photoluminescence is the strongest in spite of the reduced amount of material. This surpris- ing behavior of the photoluminescence indicates that lumi-nescence quantum efficiency is much higher in MoS2 monolayer than in multilayer and in the bulk.

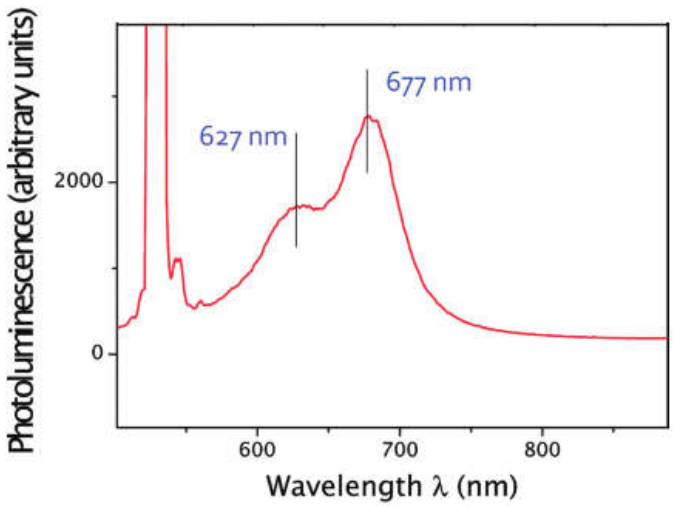

Fig. 1.4 A strong photoluminescence is observed at the direct excitonic transitions energies in a monolayer MoS2. Such luminescence is absent in the indirect bandgap bulk MoS2 sample.

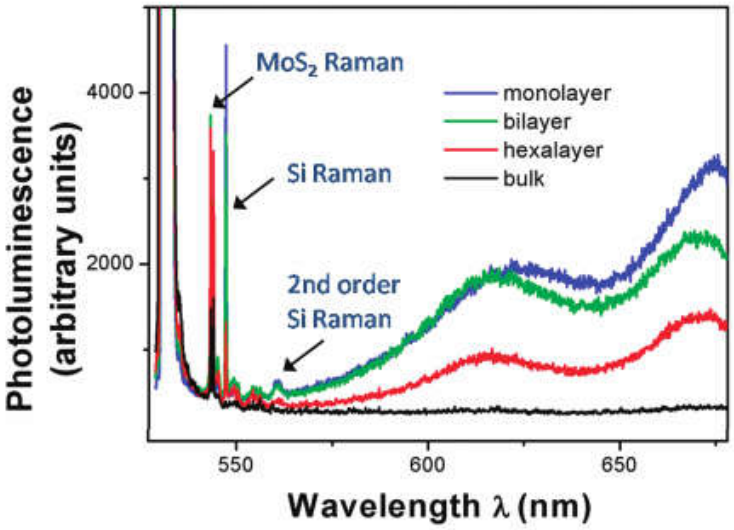

Fig. 1.5 Layer dependence of photoluminescence efficiency in MoS2. Photoluminescence and Raman spectra of MoS2 monolayer, bilayer, hexalayer, and bulk sample. Different Raman peaks can be assigned to the MoS2 and silicon vibration modes. For MoS2 thin layers, monolayer MoS2 Raman signal is relatively weak because less material is being excited. However, photoluminescence is the strongest in monolayer MoS2 in spite of reduced material.

4- Fabrication method, few and monolayer fabrication techniques

Many fabrication procedures have been developed in order to obtain few-layer TMDs, which have evolved from graphene processing strategies. These can be divided into exfoliation and growth techniques.

Exfoliation involves cleaving monolayer or few-layer flakes from a bulk crystal, typically achieved mechanically (e.g. using Scotch-tape technique [16]), chemically (e.g. lithium-based

intercalation) or through dispersal in solvents (known as LPE, liquid-phase exfoliation). Compared to micromechanical cleavage and chemical vapor deposition, liquid-phase exfoliation provides a scalable manufacturing route for high-quality layers, which is beneficial for synthesizing printable inks and functionalizing the materials in solution phase. Liquid-phase exfoliation also enables deposition on arbitrary substrates.

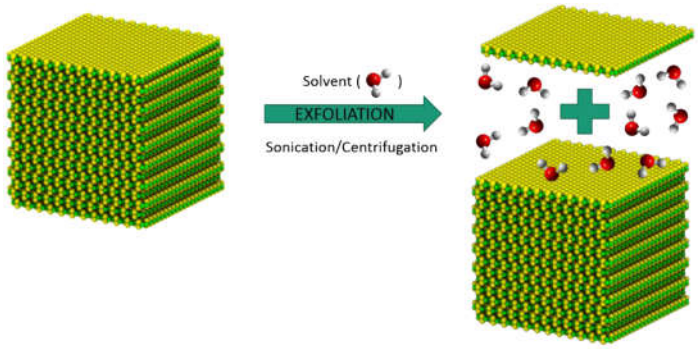

Fig. 1.6 A sketch of the liquid phase exfoliation process, showing the solvent molecules (water in this case) penetrating between the sheets of bulk molybdenum disulfide (MoS2).

Alternatively, growth techniques, such as the Chemical Vapour Deposition (CVD), can produce high-quality, single layers of the material from carefully controlled chemical reactions between solid precursors.

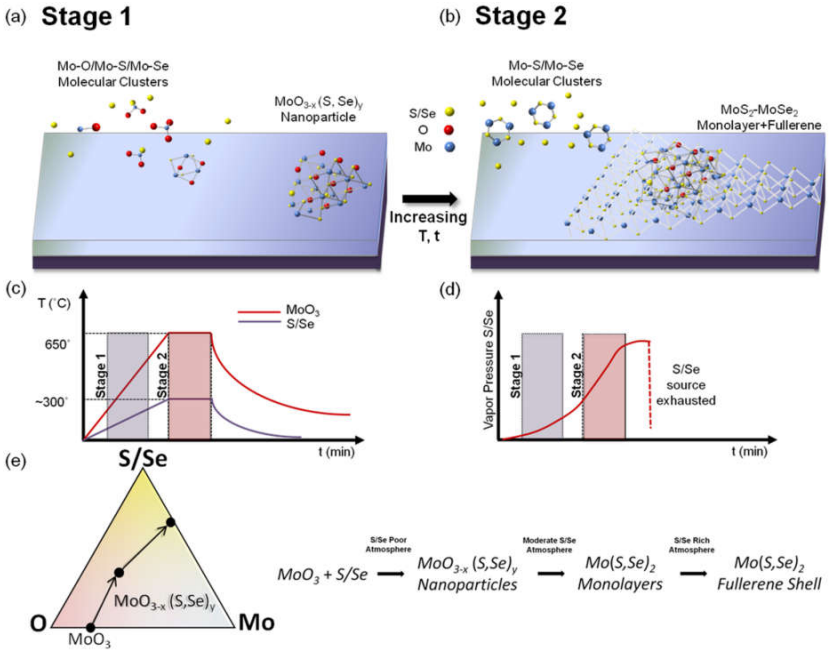

Fig. 1.7 Schematic showing the proposed nucleation and growth dynamics during (a) stage 1 and (b) stage 2. (c) Time vs temperature profile for growth. Stage 1 shows the nucleation of suboxide nanoparticles onto the substrate, and stage 2 shows the growth of the ML-TMD and fullerene shell. (d) Schematic of the S/Se vapor pressure as a function of growth time. (e) Schematic of the molybdenum-oxygen- chalcogen ternary phase diagram [**17**].

Both LPE and CVD approaches have the potential for large-scale production, which is desirable for developing saturable absorbers and photonic devices commercially. CVD typically has a higher yield of large-area monolayer flakes of TMDs, while LPE produces smaller area, few-layer flakes. The flake size is an important parameter in determining the optical properties of a single TMD device. In fact, this flake-size-dependence of the optical properties offers a convenient method for engineering the materials inexpensively using LPE.

The MoS2 dispersion contained a distribution of flake thicknesses (measured using AFM 6), and notably, 50% of flakes had a 2–4 nm thickness, which corresponds to 4–5 layers, with lateral flake dimensions typically < 200 nm [12].

5- Electronic Band structure of TMDs

Semiconducting transition metal dichalcogenides present a complex electronic band structure with a rich orbital contribution to their valence and conduction bands. A single layer of TMDs as shown in Fig **1.3**, is composed by an inner layer of metal M atoms ordered on a triangular lattice, which is sandwiched between two layers of chalcogen X atoms placed on the triangular lattice of alternating hollow sites. We use a notation such that a corresponds to the distance between nearest neighbor in-plane M–M and X–X atoms, b is the nearest neighbor M–X separation and u is the distance between the M and X planes. The MX_2 crystal forms an almost perfect trigonal prism structure with $b \simeq \sqrt{7/12}a$ and $u \simeq a/2$. The lattice parameters of the bulk compounds corresponding to the more commonly studied TMDs are given in Table **1** [18]. The in-plane Brillouin zone is a hexagon, and it is shown in Figure **1.8**. It contains the high-symmetry points $\Gamma = (0,0)$, $K = 4\pi/3a(1,0)$ and $M = 4\pi/3a(0,\sqrt{3}/2)$. The six Q points correspond to the approximate position of a local minimum of the conduction band.

	a	u	c'
MoS_2	3.160	1.586	6.140
$MoSe_2$	3.288	1.664	6.451
WS_2	3.153	1.571	6.160
WSe_2	3.260	1.657	6.422

Table 1. Lattice parameters for the TMDs (transition metal dichalcogenides) considered in the text. a represents the M–M atomic distance, u the internal vertical separation between the M and the X planes, and c' the distance between the metal M layers. In bulk systems, $c = 2c'$ accounts for the z-axis lattice parameter. All values are in Å units.

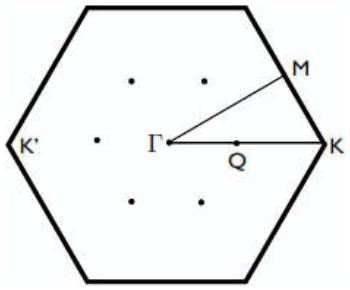

Figure 1.8. Two-dimensional Brillouin zone (BZ) of MX_2. The high symmetry points $\Gamma = (0,0)$, $K = 4\pi / 3a(1,0)$ and $M = 4\pi / 3a(0,\sqrt{3}/2)$ are shown. The Q points (which are not high symmetry points) indicate the position of the edges of the conduction band in multi-layer samples.

Figure 1.9, shows the band structures for single-layer MX_2 (black lines) together with the TB bands (red lines), black line are calculated by using the density functional theory (DFT) calculations while red lines are calculated using tight binding model.

One of the main characteristics of TMDs is that, contrary to what happens in other 2D crystals like graphene or phosphorene, the valence and conduction bands of MX_2 present a very rich orbital contribution. As explained in detail in Reference [19,20], they are made by hybridization of the d orbitals of the transition metal, and the p orbitals of the chalcogen.

Single-layer TMDs are direct gap semiconductors, with the gap located at the two inequivalent K and K' points of the Brillouin zone (Figure **1.8**).

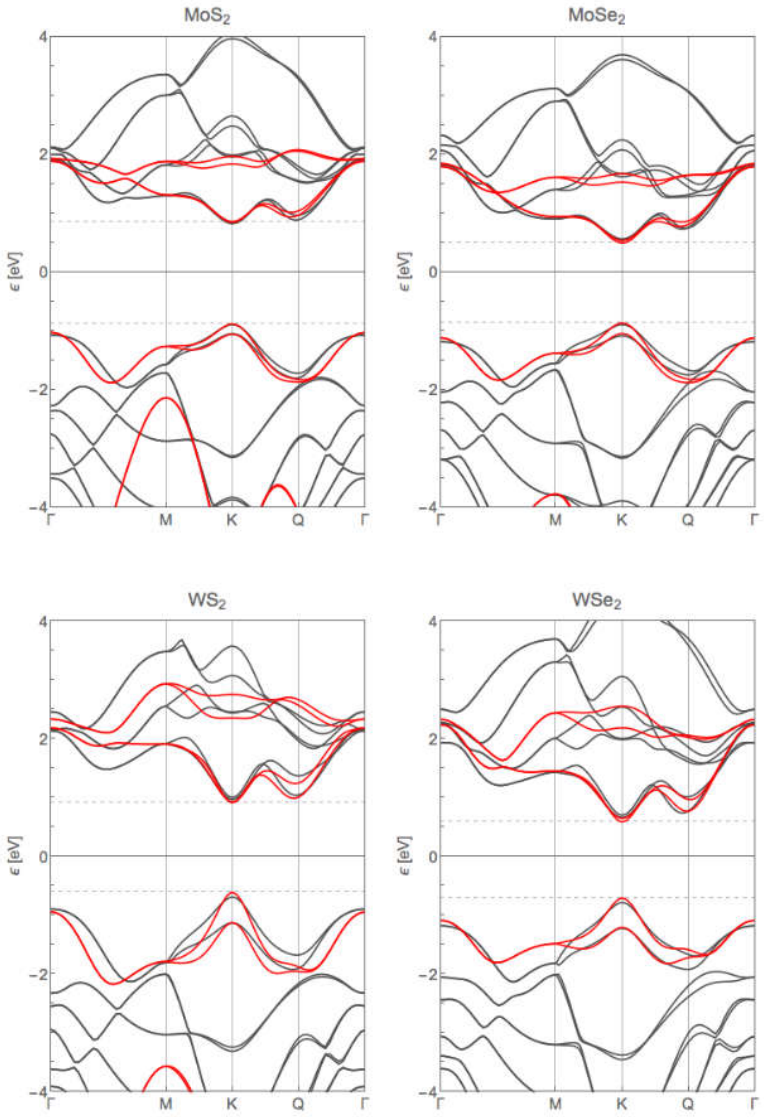

Figure 1.9. Electronic band structure of single-layer MX_2 from Density Functional Theory (DFT) calculations (black lines) and from tight-binding (TB) (red lines).

Contrary to single-layer samples, multi-layer compounds are indirect gap semiconductors. The edge of the valence band lies at the Γ point of the BZ, having a major contribution from $d_{3z^2-r^2}$ and p_z orbitals of M and X atoms, respectively. The edge of the conduction band in multi-layer samples is placed at the Q point of the BZ. It is important to notice that the Q point is not a high symmetry point of the Brillouin zone, and therefore its exact position depends on the number of layers and on the specific compound.

Another important feature of TMDs is that they present a strong SOC, which leads to a large splitting of the valence band at the K and K' points of the BZ (see Figure **1.9**). The splitting is bigger for W than for Mo compounds, due to the heavier mass of the former. SOC also leads to a splitting of the conduction band at the K point, as well as at the minimum at the Q point [**18**].

Chapter 2

Excitons in ML- TMDs

The traditional picture of optical absorption processes is described by an impinging radiation field exciting an electron-hole (e-h) pair. In the framework of the one-electron approximation, the properties of both the electron and the hole are described by the band structure. When describing complex systems this picture may not be enough. For this reason, it is necessary to go beyond this approximation, and to consider the effects of electron-electron interaction, which is essential to give an exhaustive and quantitative description of the optical processes.

We make the following assumptions:

- only the Coulomb part of e-e interaction is included (exchange and correlation terms are neglected);
- the interaction between the excited electron in the conduction band and the left ones in the (now almost filled) valence band will be replaced by an e-h interaction;
- attraction between the e and the h causes their motion to be correlated and the resultant e-h pair is a bound-state quasiparticle known as exciton.

For strong e-h attraction (i.e. ionic crystals) the electron and the hole are tightly bound to each other within the same or nearest-neighbor unit cells, these are called Frenkel Excitons. In most semiconductors the electrons and the holes are weakly bound because the Coulomb interaction is screened by the valence electrons via the large dielectric constant, and they are called Wannier-Mott Excitons.

Because of the 2D character of ML-TMDs the Coulomb interaction among the electrons is strongly enhanced. The resulting formation of bound electron-hole pairs can dominate the optical and transport properties, for this reason this work is mainly focused on the investigation of the excitonic dynamics of TMD semiconductors, MoSe2 and WS2. A microscopic view of how excitons are formed from free carriers is crucial for understanding the many-body physics in ML-TMDs [**12**].

In addition to the strong Coulomb interaction in ML TMDs, the crystal symmetry and orbital character of the bands are responsible for the underlying spin-valley properties and optical selection rules. Bulk TMDs in the semiconducting 2H phase consist of X-M-X building blocks with weak van-der-Waals bonding between the layers and are characterized by the D_{6h} point symmetry group for stoichiometric compounds. In bulk TMDs, the indirect band gap corresponds to the transition between the valence band maximum (VBM) at the center of the hexagonal Brillouin zone (Γ point) and the conduction band minimum (CBM) situated nearly halfway along the $\Gamma - K$ direction. The electronic states at the Γ point contain contributions from the p_z orbitals of the chalcogen atom and the d_{z^2} orbitals of the transition metal. In contrast, the $K^{\pm}$ point conduction and valence band states at the corners of the hexagonal Brillouin zone are

very strongly localized in the metal atom plane, as they are composed of transition metal atom $d_{x^2-y^2} \pm id_{xy}$ states (VB) and d_{z^2} states (CB) slightly mixed with the chalcogen $p_x \mp ip_y$ orbitals. The spatial overlap between adjacent MX_2 layers of the orbitals corresponding to the Γ point (VB) and the midpoint along $\Gamma - K$ (CB) is considerable. As a result, in progressing from bulk crystals to few layer samples and eventually to monolayers, the indirect gap energy corresponding to the separation between Γ and the midpoint along $\Gamma - K$ increases whereas the $K^{\pm}$ point CB and VB energies are nearly unaffected. In the ML limit, the semiconductor undergoes a crossover from an indirect to a direct gap, the later situated at the $K^{\pm}$ points (see Fig. 2b), and resulting in much stronger light emission for MLs as compared to bulk and bilayers.

As compared with bulk samples, the TMD MLs are described by the lower symmetry D_{3h} point group. The symmetry elements include a horizontal σ_h reflection plane containing the metal atoms, a threefold C_3 rotation axis intersecting the horizontal plane in the center of the hexagon, as well as a S_3 mirror-rotation axis, three twofold C_2 rotation axes lying in the ML plane, and mirror reflection planes σ_v containing the C_2 axes. The symmetry of the states at $K^{\pm}$ is still lower and characterized by the C_{3h} point group where only C_3, S_3 axes and σ_h elements are present.

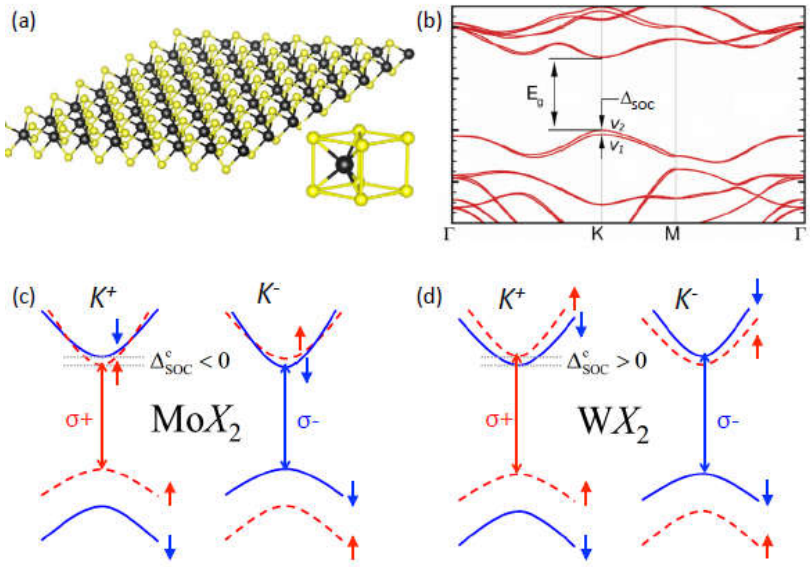

FIG. 2 (a) Monolayer transition metal dichalcogenide crystal structure. The transition metal atoms appear in black, the chalcogen atoms in yellow. (b) Typical band structure for MX_2 monolayers calculated using Density Functional Theory (DFT) and showing the quasiparticle band gap E_g at the K points and the spin-orbit splitting in the valence band. (c) Schematic in a single-particle picture showing that the order of the conduction bands is opposite in MoX_2 and WX_2 monolayers. The contribution from Coulomb exchange effects that must be added to calculate the separation between optically active (bright - spin allowed) and optically inactive (dark - spin forbidden) excitons is not shown.

The spin-orbit interaction in TMDs is much stronger than in graphene, the most prominent 2D material. The origin of this distinction lies simply in the relatively heavy elements in the TMDs

and the involvement of the transition metal d orbitals. In monolayer TMDs, the spin splitting at the K point in the valence band is around 200 meV (Mo-based) and 400 meV (W-based). This coupling gives rise to the two valence subbands and, accordingly, to two types of excitons, A and B, which involve holes from the upper and lower energy spin states, respectively. At the CBM, a smaller, but significant spin splitting is also expected due to partial compensation of the $p-$ and $d-$ states contributions. Interestingly, depending on the metal atom (Mo or W), the conduction band spin splitting has a different sign, as indicated in Fig. 2c, d. Hence, at the K point, the spin degeneracy of both the conduction and valence bands is fully lifted. This stands in marked contrast to typical GaAs or CdTe quantumwell structures where the CBM and VBM occur at the Γ point and both the conduction and valence band states remain spin degenerate. The CB spin splitting results in an energy separation between the spin-allowed and optically active (bright) transitions and the spin-forbidden and optically inactive transitions (dark). The exact amplitude of the splitting for exciton states will also depend on the contribution from the electron-hole Coulomb exchange energy. The lowest energy transition in MoX_2 is expected to be the bright exciton, which is consistent with temperature dependent PL measurements, although recent studies discuss the possibility of the ground state in $ML-MoX_2$ being dark. In contrast for the WX_2 materials, dark excitons are predicted to be lower energies, in agreement with temperature dependent studies, measurements in transverse magnetic fields and experiments probing excitons with out of- plane dipole moments. The chiral optical selection rules for interband transitions in the $K^{\pm}$ valleys can be deduced from symmetry arguments: The orbital Bloch functions of the VB states at $K^{\pm}$ points are invariants, while the CB states transform like the states with angular momentum components of ± 1, i.e., according to the E_1'/E_2' irreducible representations of the C_{3h} point group. Therefore, the optical selection rules for the interband transitions at $K^{\pm}$ valleys are chiral: the $\sigma^+(\sigma^-)$ circularly polarized light can only couple to the transition at $K^+(K^-)$.This permits the optical generation and detection of the spinvalley polarization, rendering the TMD monolayers an ideal platform to study the electron valley degree of freedom in the context of valleytronics. In that context, it is important to emphasize, that for an electron to change valley, it has either to flip its spin (see Fig. 2c, d) or undergo an energetically unfavorable transition, especially for the valence states. As a result, optically generated electrons and holes are both valley and spin polarized, which is termed *spin-valley locking*. Therefore, following the σ^+ excitation, the exciton emission in TMD MLs can be co-polarized with the laser if the *valley* polarization lifetime is longer or of the order of the recombination time. This behavior stands in contrast to that of III-V or II-VI quantum wells where excitation with the circularly polarized light usually results only in spin-polarization of the charge carriers [20].

Chapter 3

OPA and NOPA techniques, Experimental procedures

In this thesis work two different types of pump-probe experiments were performed: single color degenerate and broadband transient absorption experiments. In order to study the non-equilibrium optical response of atomically thin flakes of TMDs we have performed these experiments on a μm spatial scale combining the pump-probe setup with an optical microscope. The pump-probe setup is seeded by a amplified Ti:sapphire laser (Coherent Libra 2) emitting a train of 100 fs pulses centered around $\lambda = 800nm$ at a repetition rate of 2 KHz. The average power is 4W, i.e. 2 mJ per pulse.

3.1 Degenerate pump-probe setup

In the degenerate pump-probe setup (see Fig. 3.2) the fundamental wavelength is split in two parts, with the same intensity, seeding two white-light-seeded second-harmonic-pumped broadband Non-collinear Optical Parametric Amplifiers (NOPA), which are going to become the pump and the probe, respectively. Due to the non-linear optical processes is possible to tune the output of these NOPAs (i.e the pump and probe beams) over a broad energy range spanning the visible-near-IR range.
The probe is further split into two parts, one is sent to a reference photodetector (PD) and the other is focused onto the sample. The back scattered (in reflection geometry), or the transmitted (in transmission geometry), probe light is then recorded by another signal PD.

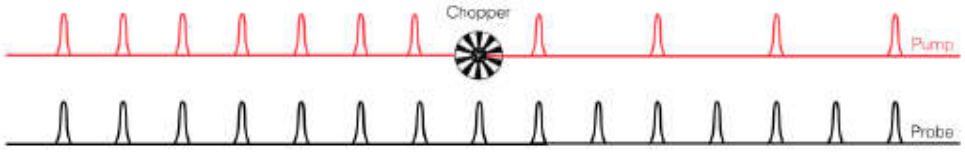

Figure 3.1: The chopper on the pump beam suppresses one pump pulse each two pump pulses.

The pump is temporally delayed with respect to the probe beam by a mechanical delay stage. The pump beam, before being focused onto the sample, is modulated at the 1 kHz frequency by a mechanical chopper (see Fig. 3.1) in order to suppress background light and low frequency noise. It is also possible to modulate the pump at higher frequency by using acusto or electro optic modulator. A broadband halfwave plate is used rotate the polarization. This configuration allows to eliminate the scattered light of the pump beam.

Pump and probe beams are collinearly sent onto a short focal length lens which focuses them onto the sample.

Degenerate Detection System

The probe beam, after been reflected or transmitted by the sample, is collected at different delay intervals onto a photodetector (PD), implemented as an integrator operational amplifier, with a time constant $RC = \tau = 50ms$. While integrating, this time constant avoids the pile-up of pulses, since laser pulses have a repetition rate of 2 KHz (i.e. a temporal distance pulse to pulse of 500 ms). The Si-based active element of the sensor allows to collect light up to $1.1\mu m$. In

order to extract the pump-probe signal, modulated at 1 KHz, we use a high-speed digitizer from National Instrument (NI PCI-5122) capable of 100 MS/s real-time, 2.0 GS/s random interleaved sampling and 100 MHz bandwidth. The digitizer makes use of 14-bit analog-to-digital converters (ADCs) and it is characterized by low-noise
variable-gain amplifier.

$$\frac{\Delta T}{T} = \frac{T^{probe}_{PUMP-ON} - T^{probe}_{PUMP-OFF}}{T^{probe}_{PUMP-OFF}} = \frac{T^{probe}_{PUMP-ON}}{T^{probe}_{PUMP-OFF}} - 1 \qquad (3.1)$$

We integrate over 80 couples of pulses, using a sampling frequency of 37 MHz, in order not to saturate the internal memory of the digitizer (the maximum sampling frequency achievable is 100 MHz). The temporal sampling axis is divided in 50000 sampling points in which we detect a couple of probe pulses (the two pulses are the probe transmitted by the pump-excited and unperturbed sample, $T^{probe}_{PUMP-ON}$ and $T^{probe}_{PUMP-OFF}$. We digitally subtract two consecutive pulses ($T^{probe}_{PUMP-ON}$ and $T^{probe}_{PUMP-OFF}$), normalizing on the value of $T^{probe}_{PUMP-OFF}$ (see Eq. 3.1). With such a configuration we can reach sensitivities of $10^{-3} - 10^{-4}$.
The main noise sources in a pump-probe detection system are laser excess noise[1], shot noise, and electronic noise of the detectors and the data acquisition device. The laser excess noise is the dominant part. In order to further improve the signal to noise ratio .we used a second PD collecting in parallel the train of probe pulses before reaching the sample. In this way we could normalize with respect to the reference pulses, $T^{probe-ref}_{PUMP-ON}$ and $T^{probe-ref}_{PUMP-OFF}$, respectively.
Eq. (3.1) becomes (3.2) and with such configuration we drastically reduce the intrinsic noise of the laser beam and the resulting S/N ratio is improved by a factor 10.

$$\frac{\Delta T}{T} = \frac{T^{probe}_{PUMP-ON}}{T^{probe}_{PUMP-OFF}} \frac{T^{probe-ref}_{PUMP-OFF}}{T^{probe-ref}_{PUMP-ON}} - 1 \qquad (3.2)$$

We can reach sensitivities of the order of $10^{-4} - 10^{-5}$.

4.2 Hyperspectral (broadband) pump-probe setup

In the broadband pump-probe setup (see reflection geometry in Fig. 3.8 and transmission geometry in in Fig. 3.9) the fundamental wavelength of the laser is by a 50% dielectric beam splitter BS in two beams, the pump and the probe. Both pulses are seeds two white-light-seeded second-harmonic-pumped broadband Non-collinear Optical Parametric Amplifier (NOPA). In this configuration the pump is the output of a narrowband OPA, and it is characterized by a bandwidth of about 10 nm. The probe beam has a broad spectral content and it is generated by optical parametric amplification of WLC.
Also, in this setup pump and probe beam have cross polarizations (s and p, respectively). After the WL probe is generated, it's finally focused onto the sample.
The reflected/transmitted probe light from the sample is angularly dispersed by a prism and it's collected by an OMA (Optical Multichannel Analyzer). The probe beam is p-polarized in order to minimize the losses introduced by the dispersing prism.
Analogously to the degenerate pump-probe setup, the pump is temporal delayed with respect to the probe by a mechanical delay stage. Then it's chopped at 1KHz (see Fig. 3.1) and finally it focuses onto the sample.

Broadband Detection System

The hyperspectral detection system exploits an Optical Multichannel Analyzer (OMA) to detect the whole probe spectrum at different pump-probe delays T, thus resulting in a 2D map. The OMA consists of an array of 512 Si-based photodiodes. The single wavelength differential transmission is digitally obtained subtracting the pump-on probe spectrum to the pump-off probe spectrum with the same principle already explained in subsection Degenerate Detection System, the only difference is that this detection system is not referenced, indeed with such configuration we are able to reach sensitivities of $10^{-3} - 10^{-4}$.

Non-Collinear Optical Parametric Amplifier (NOPA)

The pump beam is frequency doubled in a BBO crystal, and the seed is the WLC continuum generated in a sapphire plate. The BBO is cut at an angle $\vartheta = 32^{\circ}$ from the crystallographic axis, such that a type I phase matching is reached in a non collinear configuration, with pump and seed angularly tilted by an angle $\psi \approx 3.8^{\circ}$.

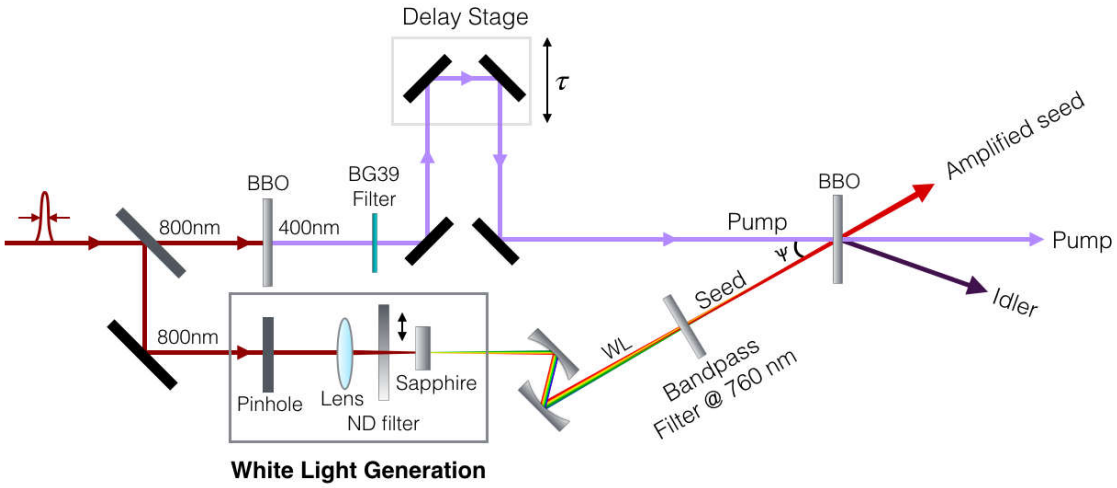

Figure 3.2: Single wavelength NOPA.

In case we need to amplify a single wavelength (see Fig. 3.2), we select by mean of an interferential filter with $10nm$ bandwidth the desired wavelength from the WLC. Experimentally, we adjust such that the seed overlaps to the super fluorescence ring, which is due to the amplification of the quantum noise emitted by the BBO when only the pump is sent through it. This super fluorescence emission is isotropic at the broadband phase matching angle and reveals as a ring when a sheet of paper is put after the BBO (see Fig. 3.4a).

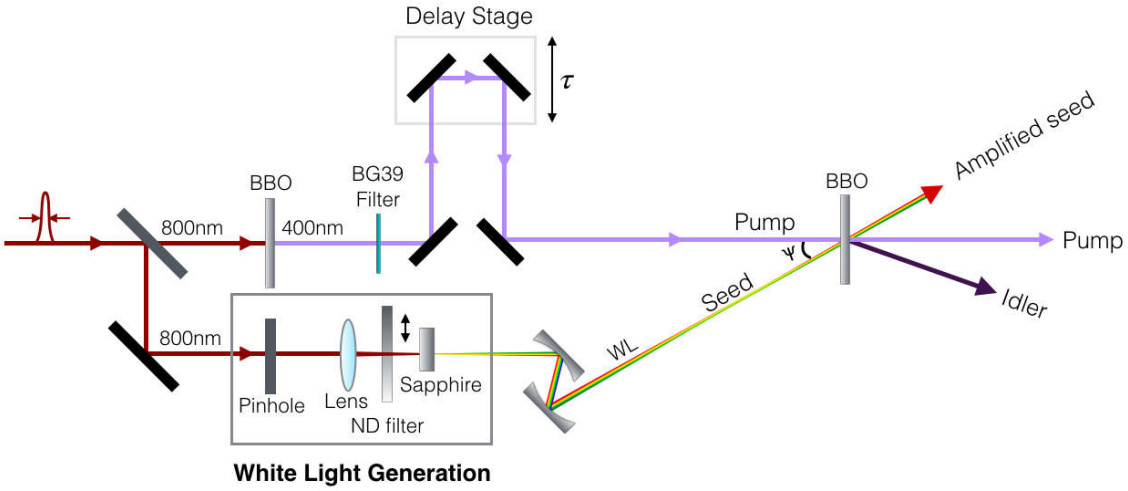

Figure 3.3: Broadband NOPA

In case we need to amplify a broadband pulse (see Fig. 3.3) the seed branch is focused onto a sapphire plate in order to generate WLC, and the generated WLC is directly sent to the BBO, where, provided that temporal and spatial overlap of pump and seed occur, the broadband amplification is obtained (in Fig. 3.4b we can see the broadband amplification of the WL on the left of the pump, and the generated different idlers at any wavelength angularly dispersed). Also, in this configuration pump and seed are angularly separated by an angle, chosen such that phase matching condition for the WL broadband amplification is reached.

Figure 3.4: (a) Pump at the center and seed (not yet amplified) overlapped to the super fluorescence ring. (b) Pump at the center and reached broadband seed amplification on the right. Observed idler formation on the right.

Microscope

One of the most challenging goals achieved in this thesis work is to couple a microscope to the preexisting pump-probe setup. In order to build this microscope, we add:

- a collimated white light source, in order to uniformly illuminate the sample, together with a flip beam splitter to send the white lamp light onto the sample;

- a flip mirror that when flipped up (and the white lamp switched off) allows the pump-probe signal detection, and when flipped down (and the white lamp switched on) allows the imaging detection of the sample, together with pump and probe beams;
- a beam splitter, just before the focusing lens f2, in order to send the backscattered light from the sample onto the camera;
- a further focusing lens f_1, in order to focus the backscattered collimated white lamp light and pump and probe beams onto the camera.

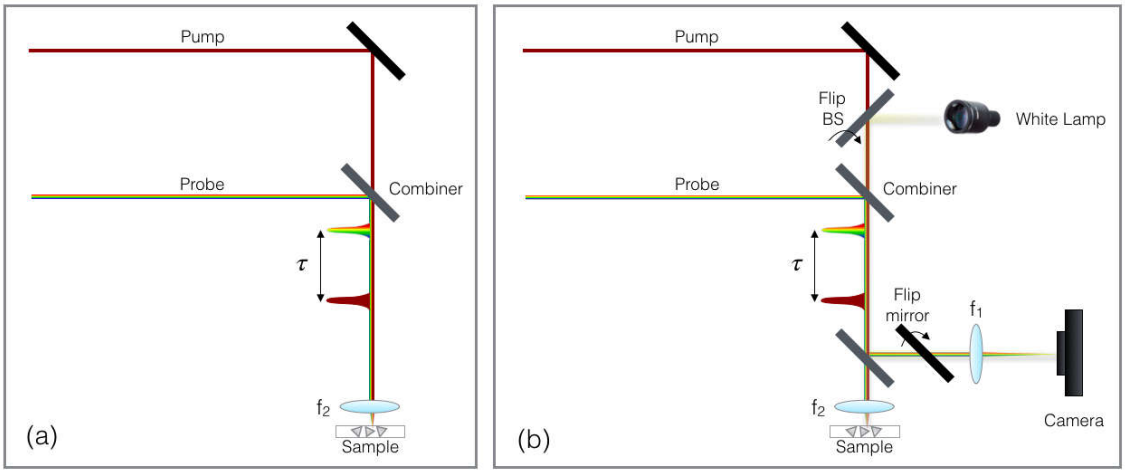

Figure 3.5: (a) Section of the pump-prope setup without and (b) with the implemented microscope.

The achieved magnification factor was:

$$M \approx \frac{f_1}{f_2} \qquad (3.3)$$

Where f_1 was always kept fixed, $f_1 = 200nm$, while different f_2 were used, like $f_2 = 50nm$ ($M \approx 4$), $30mm$ ($M \approx 7$), $8mm$ ($M \approx 25$).

The camera used to detect back scattered light is a Thorlabs Compact USB 2.0 CMOS Camera, with 1280 x 1024 pixels and an active sensor of 1/2", so each pixel size $a \simeq 5\mu m$. We extimated, both along x and y, the spot size of the beams by counting the n° of pixels associated to the FWHM of the pulse, by the following:

$$\Delta x = \frac{n^\circ_{pixels}}{M} a \qquad (3.4)$$

The estimated pump and probe spot size on the sample, using $f_2 = 50\,nm$, was $\Delta x \approx 30\ \mu m$.

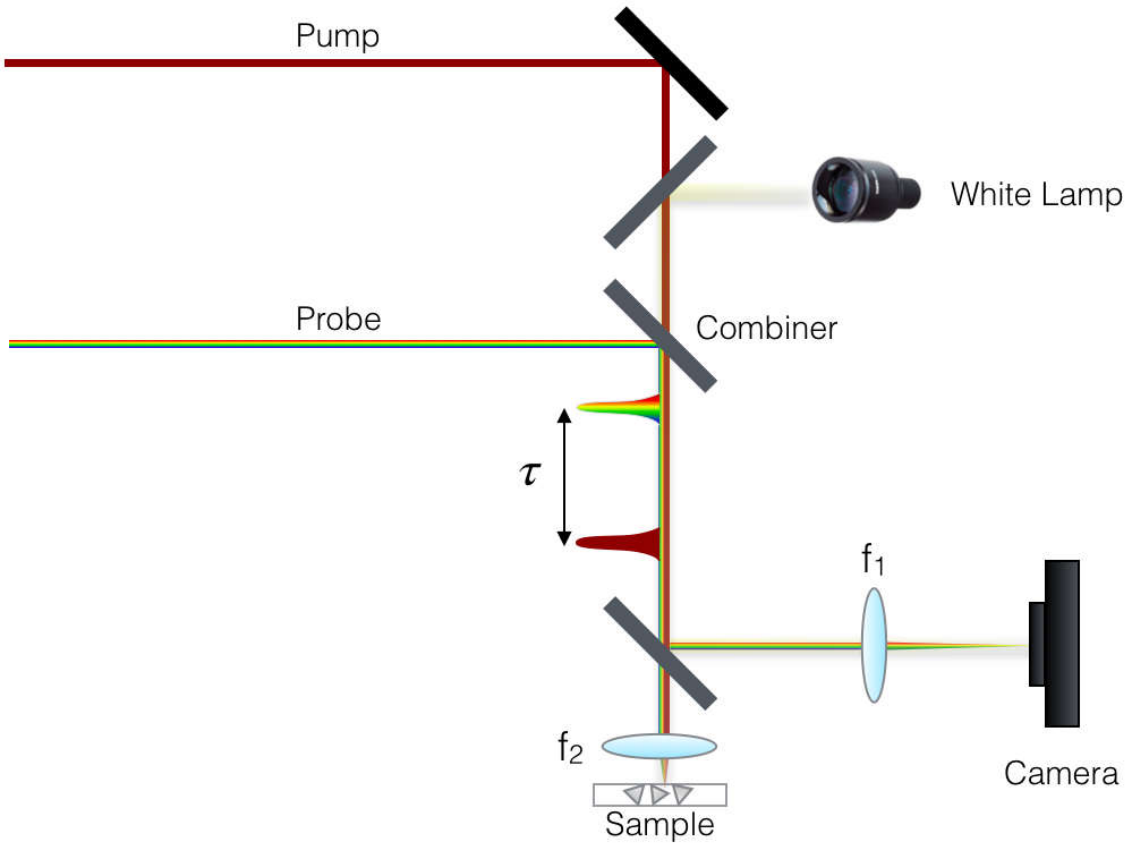

Figure 3.6: Home-built microscope configuration achieved with flipped down mirror.

One of the hardest parts of this coupled system was getting the focus of the beams and the focus of the image of the sample occurring in the same plane. In order to reach the focus we had three degrees of freedom: we could slightly slide the camera along the direction of the incoming beams; we could move a bit le lens f_2 (f_1 was always kept fixed), which was mounted on a micrometric translation stage and we could translate the sample, because its holder was mounted on a x-y-z translation stage moving in micro steps of $5\,\mu m$.

This setup allows to detect micrometric samples and to precisely direct pump and probe beams on the region to study.

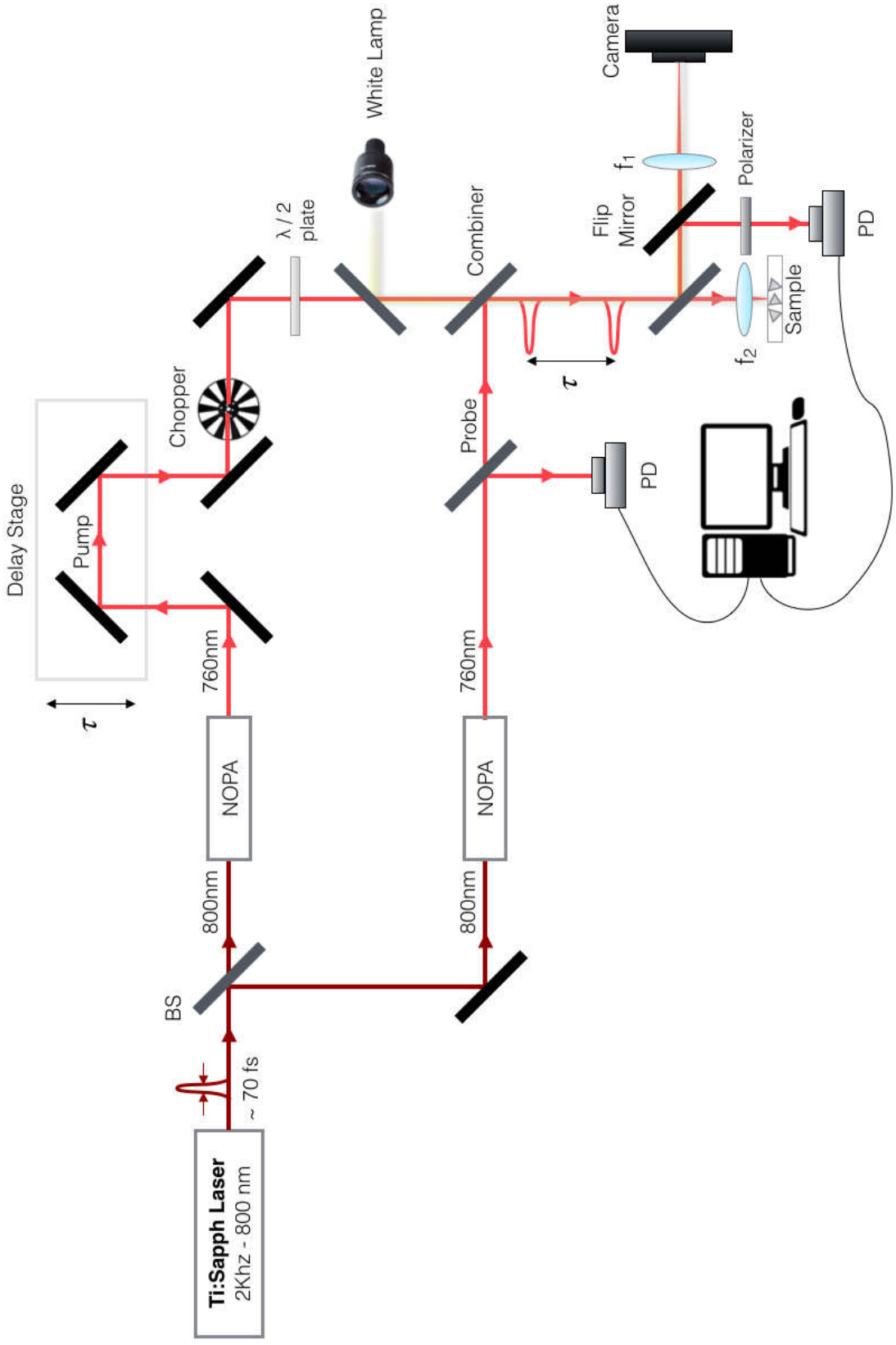

Figure 3.7: Reflection geometry degenerate pump-probe setup.

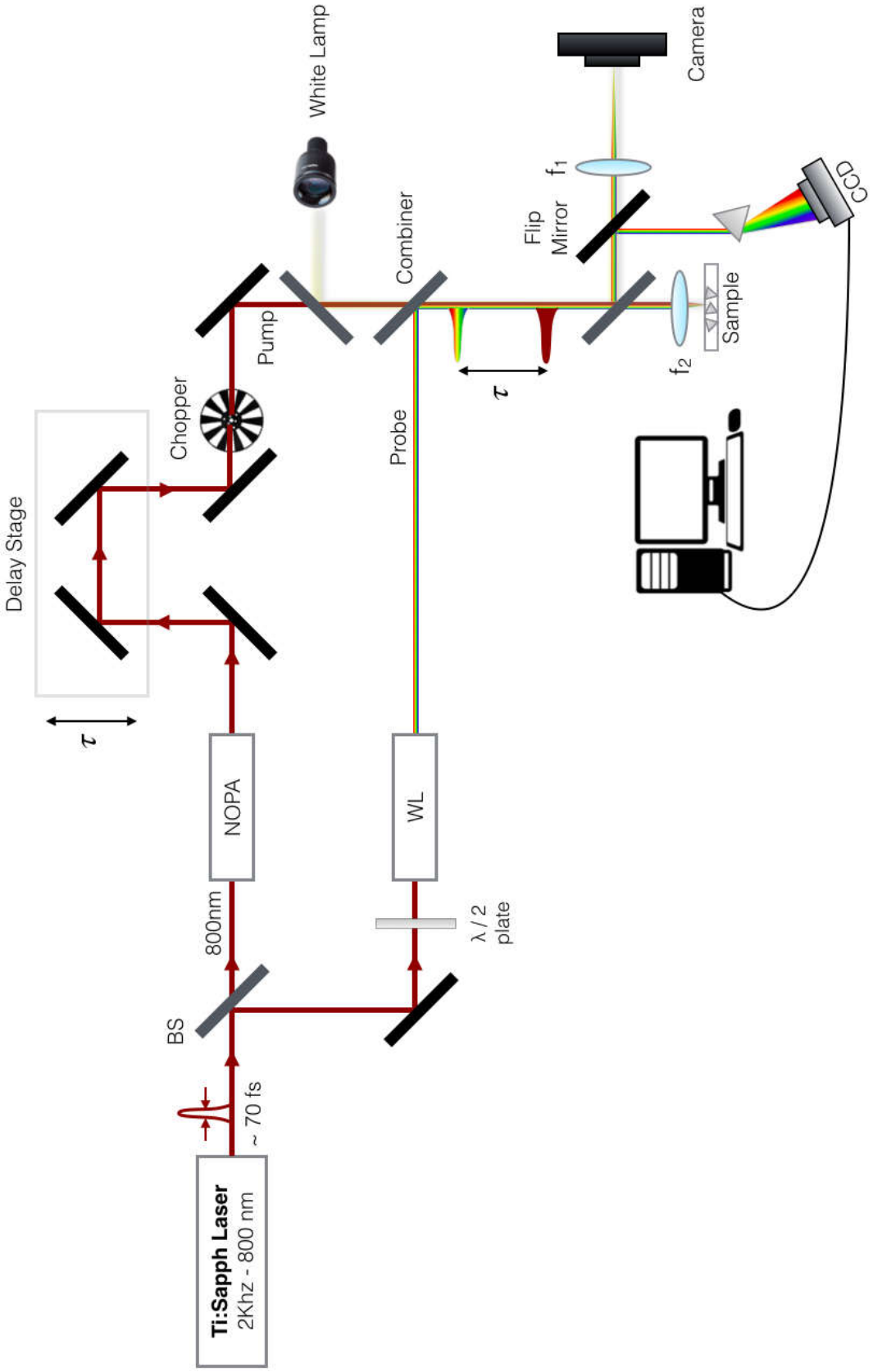

Figure 3.8: Reflection geometry hyperspectral pump-probe setup.

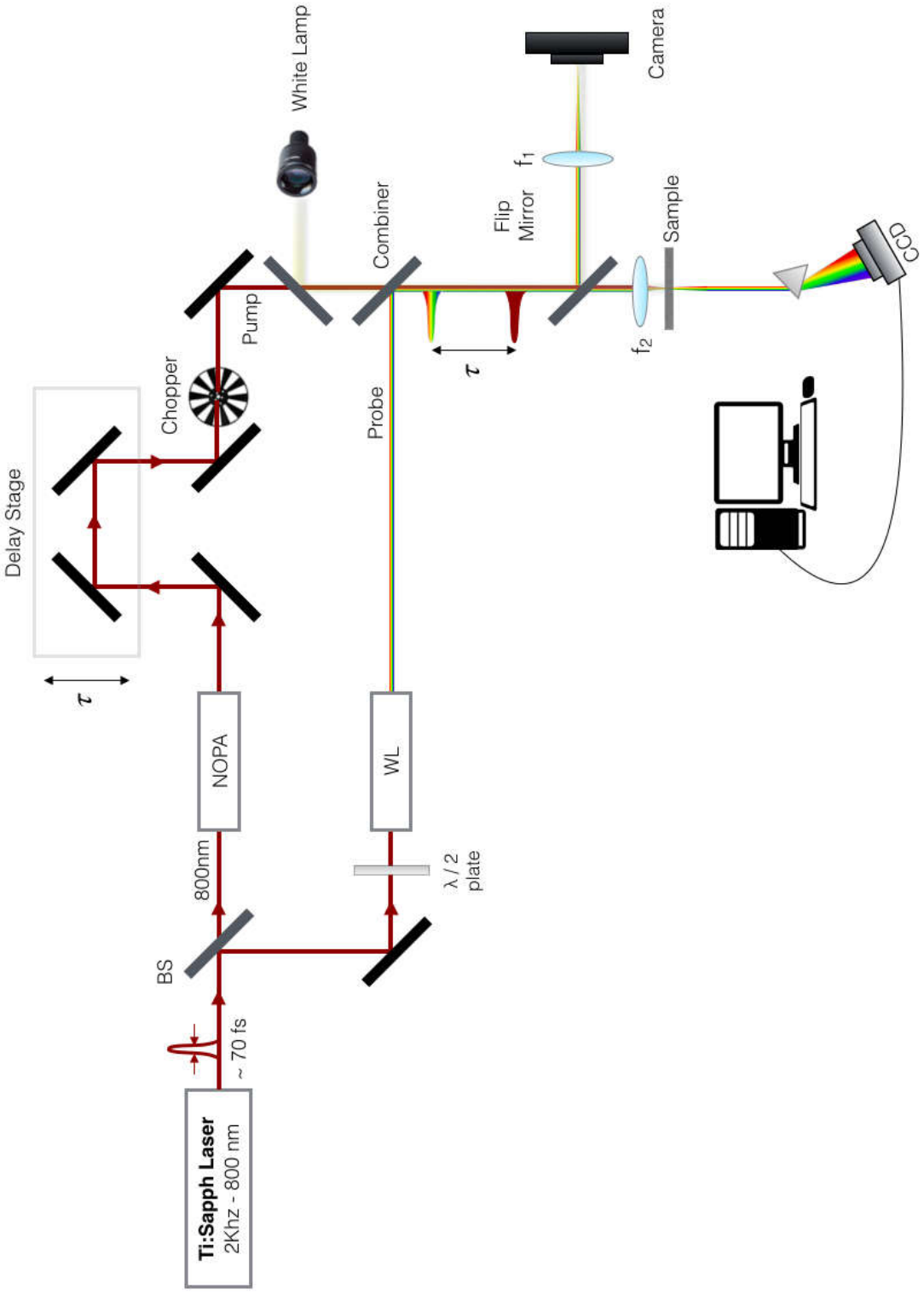

Figure 3.9: Transmission geometry hyperspectral pump-probe setup.

Chapter 4

Experimental results

in this chapter we study the relaxation dynamics of ML-MoSe2 by pump-probe spectroscopy. We performed degenerate transient absorption measurements; i.e, pump and probe pulses have the same wavelength and broadband transient absorption measurements; i.e, the pump is a narrowband pulse with 10 nm spectral bandwidth, and the probe is a white light broadband pulse covering the entire visible range.

The sample is a CVD-grown, highly crystalline ML-MoSe2. The sample is originally grown on a SiO2/Si substrate and then transfer on top of a silver substrate by a wet-transfer technique based on a sacrificial layer of poly-methyl-methacrylate (PMMA).

The main goal of the experimental work is coupling the pump-probe setup with a home-built microscope. The resulting transient optical spectroscopy setup will combine high temporal resolution (about 100 fs) and a micrometric spatial resolution of the order of $1-10\mu m$. Since the average lateral size of the monolayer flake is about $30\mu m$, we can study the transient optical response of a single flake.

In order to preserve the temporal length of optical pulses without compromising the spatial resolution, we use a focusing element short focal length achromatic lenses ($f = 50mm$).

We performed transient absorption measurements in a degenerate configuration in order to study the saturable absorption properties and the relaxation dynamics of ML-MoSe2.

ML-MoSe2 has two exitonic absorption peaks A ($\lambda \sim 700nm$) and B ($\lambda \sim 790nm$) as shown in figure 4.1.

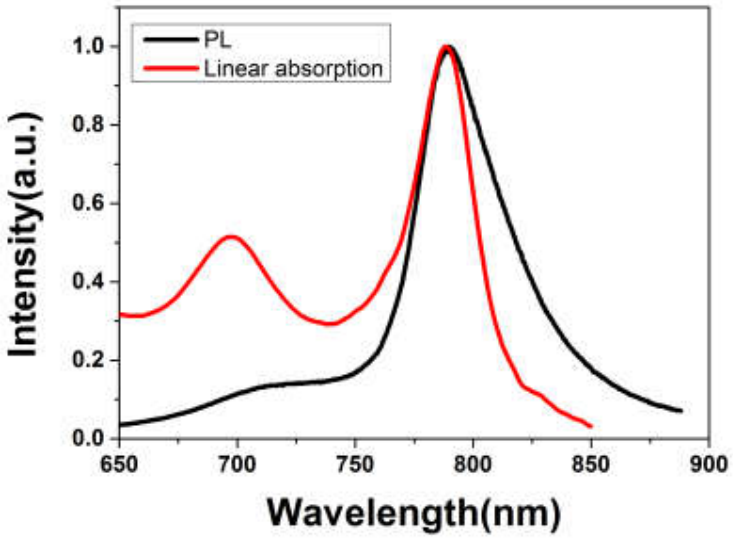

Fig 4.1: normalized linear absorption and photoluminescence for MoSe2

Degenerate pump-probe measurements were performed at different frequencies covering A and B excitonic peak. We work in a collinear reflection geometry. In this configuration, the pump beam spot diameter d is about $30\mu m$. The saturable absorption properties have been previously measured by single pulse spectroscopy (SPS) in the same group of Profs. Wang. A simplified sketch of SPS measurements shown in Figure 4.2.

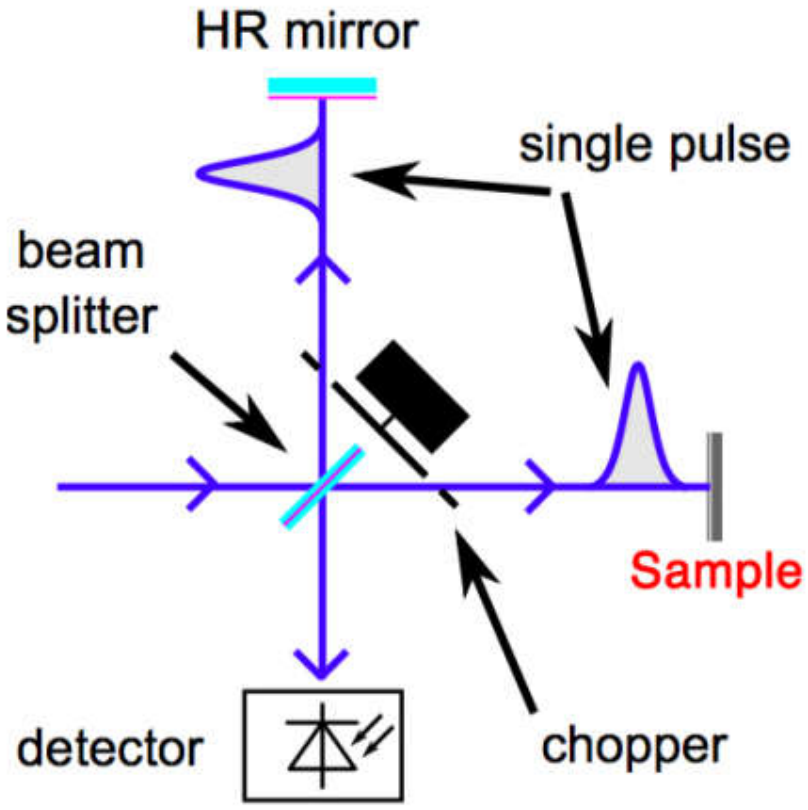

Figure 4.2: Scheme of the SPS experimental setup. In SPS a single pulse is split and incident both on a SESAM and on a highly reflective (HR) mirror.

4.2 Transient optical response

In our measurement, we analyze $\Delta T / T$ the elative transient map of ML-MoSe2 measured as a function of the delay and the probe wavelength. The $\Delta T / T$ map displays strong positive signals centered around A/B exitonic peaks of ML-MoSe2. These features are mainly ascribed to the pump induced photobleaching (PB) of the excitonic transitions due to the phase space fitting effect.

The spectrum for A and B excitons in both cases long and short delay time between pump and probe beams, are shown in Fig. 4.3, we plotted these diagrams by making average on many scans, with respect to the maximum magnitude of $\Delta T / T$ in each scan.

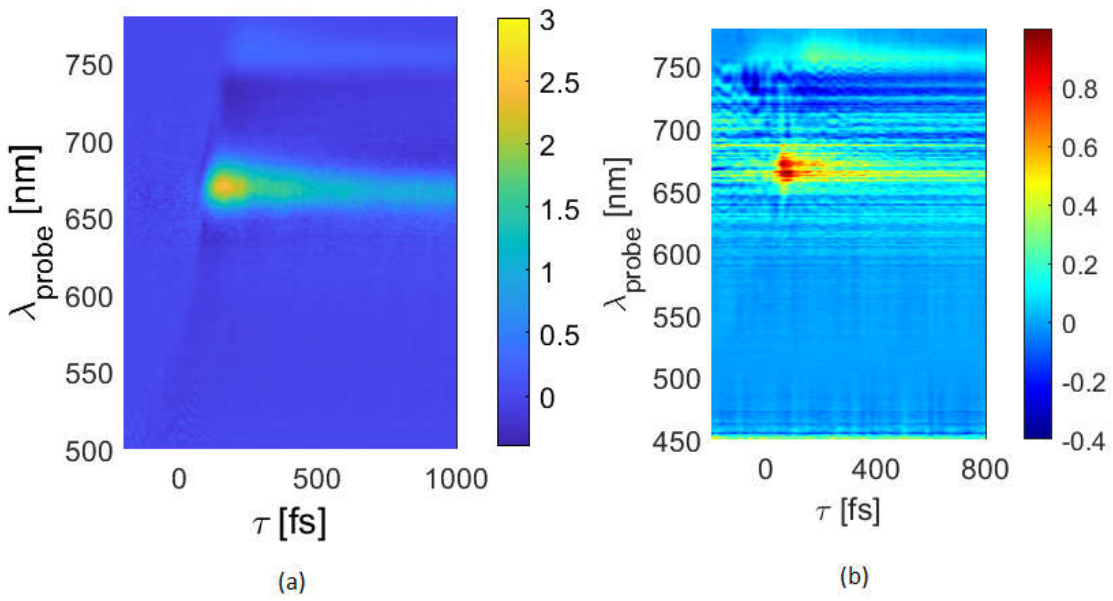

Figure 4.3: Pump Probe map. Experimental $\Delta T / T$ map of ML-MoSe2 for (a) short, (b) long delay.

Figure 4.4 shows the spectrum for two cases the same and opposite polarization of Pump and probes beams.

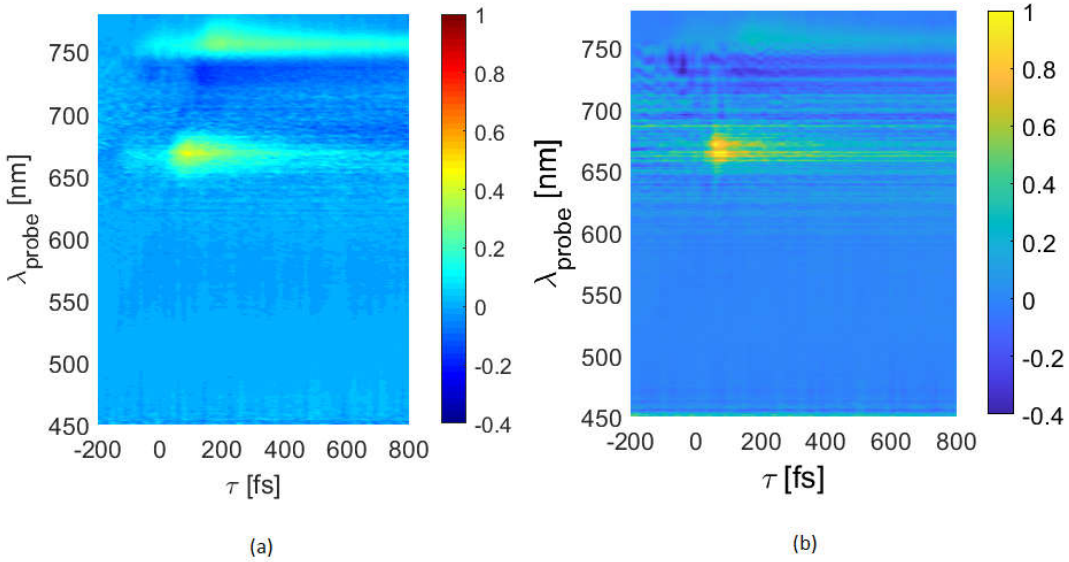

Figure 4.4: Pump-Probe maps. Experimental $\Delta T / T$ map of ML-MoSe2 for (a) the same and (b) the opposite polarization of Pump and probe beams.

To compare, two spectrums with the same and opposite polarization measurements, for the short and long delay cases, we plot the differential transient $\Delta T / T$ with respect to the wavelength of probe, for A and B excitons. Figure 4.5 shows the results.

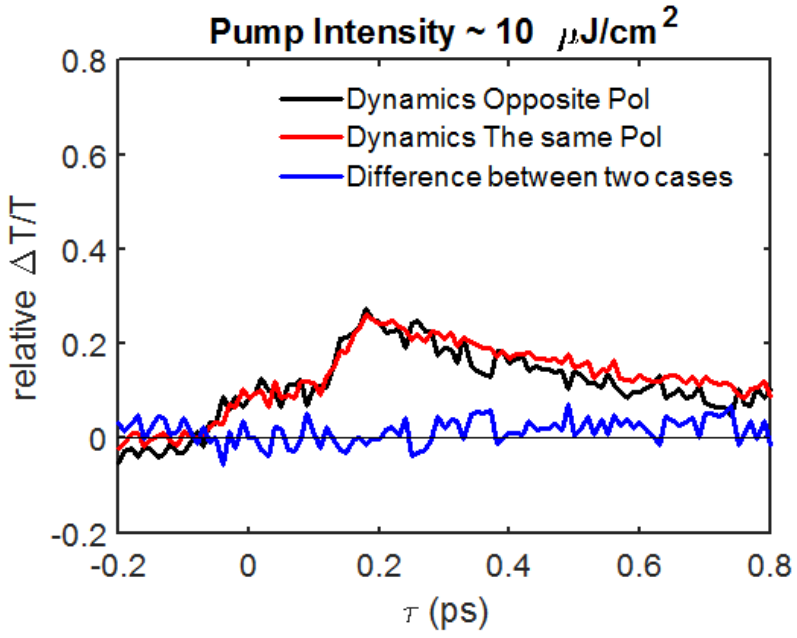

Figure 4.5: comparing two spectrums with the same and opposite polarization in a temporal delay around B exciton.

4.5 Fitting of experimental data

After evaluating spectrum for MoSe2 and comparing the measured temporal and spectral dynamics with respect to polarization and long or short delay, we evaluate the diagram $\Delta T / T$ with respect to the temporal delay for A and B excitons with the best possible fit of the data.

In fact, using MATLAB algorithm $lsqnonlin$, we fir our experimental data with a Gaussian-experimental curve. For the fitting curve we use the following function:

$$f(t) = A.\exp(-t^2 / \Delta t^2) \otimes (B.\exp(-t / \tau_1) + C.\exp(-t / \tau_2)).H(t - t0) \qquad (4\text{-}1)$$

Where the material response is modeled by a gaussian function convolve with exponential decay function, with time constant τ_1, τ_2 and A, B, C are respectively amplitudes of gaussian function and exponential decay function.

Here $A, B, C, \Delta\tau, \tau_1, \tau_2$ are the free parameters of the fir. The Heaviside function H accounts for temporal offset, t_0. Therefor we use 5 free parameters to fit the temporal dynamics on a long-time scale. Figure 4.6 shows some examples of fitting.

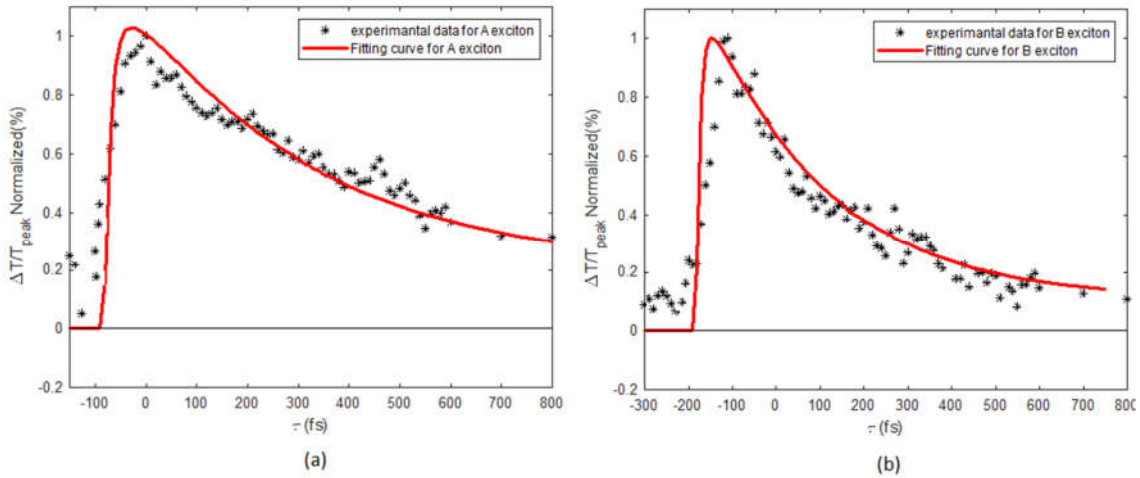

Figure 4.6: Experimental transient dynamics fit. Fit of the temporal dynamics for (a) A exciton, (b) B exciton.

References

[1] G. H. Han, D. L. Duong, D. H. Keum, S. J. Yun, and Y. H. Lee, Chem. Rev. 2018, 118, 13, 6297–6336 Publication Date:June 29, 2018,https://doi.org/10.1021/acs.chemrev.7b00618.

[2] K. S. Novoselov, A. K. Geim, S. V. Morozov, D. Jiang, Y. Zhang, S. V. Dubonos, I. V. Grigorieva, A. A. Firsov, Science (New York, N.Y.) 2004, 306, 666.

[3] K. S. Novoselov, D. Jiang, F. Schehedin, T. J. Booth, V. V. Khotkevich, S. V. Morozov, A. K. Geim, PNAS 2005, 102, 10451.

[4] K. S. Novoselov, V. I. Fal'ko, L. Colombo, P. R. Gellert, M. G. Schwab, K. Kim, Nature 2012, 490, 192.

[5] M. Peplow, Science, 2013, New york, 503, 327.

[6] D. Akinwande, N. Petrone, J. Hone, Nature communications 2014, 5, 5678.

[7] G. Fiori, F. Bonaccorso, G. Iannaccone, T. Palacios, D. Neumaier, A. Seabaugh, S. K. Banerjee, L. Colombo, Nature nanotechnology 2014, 9, 768.

[8] U. Wurstbauer, B. Miller, E. Parzinger, and A. W. Holleitner, Light matter interaction in transition metal dichalcogenides and their heterostructures, 2017, J. Phys. D: Appl. Phys. 50 173001.

[9] A. V. Kolobov, J. Tominaga , Two-Dimensional Transition-Metal Dichalcogenides, (Springer, Switzerland 2016), DOI 10.1007/978-3-319-31450-1.

[10] Eva A. A. Pogna, M. Marsili, D. D. Fazio, S. D. Conte, C. Manzoni, D. Sangalli, D. Yoon, A. Lombardo, A. C. Ferrari, A. Marini, G. Cerullo, and D. Prezzi, Photo-Induced Bandgap Renormalization Governs the Ultrafast Response of Single-Layer MoS2, 2015 American Chemical Society, DOI: 10.1021/acsnano.5b06488 ACS Nano 2016, 10, 1182−1188.

[11] Wang, R.; Ruzicka, B. A.; Kumar, N.; Bellus, M. Z.; Chiu, H.-Y.; Zhao, H. Ultrafast and Spatially Resolved Studies of Charge Carriers in Atomically Thin Molybdenum Disulfide. Phys. Rev. B: Condens. Matter Mater. Phys. 2012, 86, 45406.

[12] C. TROVATELLO, Ultrafast carrier relaxation dynamics in two-dimensional Semiconductors, Master of Science Thesis Work, 2016, Politecnico di Milano.

[13] C. Chakraborty, L. Kinnischtzke, K. M. Goodfellow, R. Beams, A. N. Vamivakas, Nature nanotechnology 2015, 10, 507.

[14] K. S. Novoselov, A. K. Geim, S. V. Morozov, D. Jiang, Y. Zhang, S. V. Dubonos, I. V. Grigorieva, A. A. Firsov, Science ,New York, 2004, 306, 666.

[15] G. Fiori, F. Bonaccorso, G. Iannaccone, T. Palacios, D. Neumaier, A. Seabaugh, S. K. Banerjee, L. Colombo, Nature nanotechnology 2014, 9, 768.

[16] K. S. Novoselov, A. Mishchenko, A. Carvalho, Castro Neto, A H, Science (New York, N.Y.) 2016, 353.

[17] K. F. Mak, C. Lee, J. Hone, J. Shan, T. F. Heinz, Physical review letters 2010, 105, 136805.

[18] A. Splendiani, L. Sun, Y. Zhang, T. Li, J. Kim, C.-Y. Chim, G. Galli, F. Wang, Nano letters 2010, 10, 1271.

[19] B. Radisavljevic, A. Radenovic, J. Brivio, V. Giacometti, A. Kis, Nature nanotechnology 2011, 6, 147.

[20] G. Wang, A. Chernikov, M. M. Glazov, T. F. Heinz, X. Marie, T. Amand and B. Urbaszek, Excitons in atomically thin transition metal dichalcogenides, arXiv:1707. 10 Nov 2017.

[21] C. R. Dean, A. F. Young, I. Meric, C. Lee, L. Wang, S. Sorgenfrei, K. Watanabe, T. Taniguchi, P. Kim, K. L. Shepard, J. Hone, Nature nanotechnology 2010, 5, 722.

[22] Q. H. Wang, K. Kalantar-Zadeh, A. Kis, J. N. Coleman, M. S. Strano, Nature nanotechnology 2012, 7, 699.

[23] Y. Yoon, K. Ganapathi, S. Salahuddin, Nano letters 2011, 11, 3768

[24] . Cappelluti, E.; Roldán, R.; Silva-Guillén, J.A.; Ordejón, P.; Guinea, F. Tight-binding model and direct-gap/indirect-gap transition in single-layer and multilayer MoS2. Phys. Rev. B 2013, 88, doi:10.1103/PhysRevB.88.075409.